scientific reports

Check for updates

OPEN

Quantitative evaluation of particle–binder interactions in ceramic slurries via differential centrifugal sedimentation

Hideaki Nakajima[1]✉, Toshihiko Ogura[2], Yuichi Kato[3], Naoki Kondo[4], Ryutaro Usukawa[4], Ryota Watanabe[5], Kazufumi Kobashi[1] & Toshiya Okazaki[1]✉

In diverse materials science spanning from fine ceramics to lithium-ion batteries and fuel cells, the particle–binder interactions in slurries play a crucial role in governing the ultimate performance. Despite numerous efforts to date, quantitatively elucidating these hidden interactions has remained a longstanding challenge. Here, we demonstrate a dynamic approach to evaluate adsorptive interactions between ceramic particles and polymeric binders entangled in a slurry utilizing differential centrifugal sedimentation (DCS). Particles settling under a centrifugal force field impart significant viscous resistance on the adsorbed binder, leading to its detachment, influenced by particle size and density. This behaviour directly reflects the particle–binder interactions, and detailed DCS spectrum analysis enables the quantitative assessment of nano-Newton-order adsorption forces. An important finding is the strong correlation of these forces with the mechanical properties of the moulded products. Our results provide insight that forming a flexible network structure with appropriate interactions is essential for desirable formability.

One of the most longstanding concerns for the science of slurry is the quantitative understanding of its characteristics. In various materials science such as fine ceramics[1–3], lithium-ion batteries[4–6], and fuel cells[7,8], the liquid-phase process is a versatile manufacturing method, and slurries (also known as suspension or ink) serve as the starting materials. Generally, slurries consist of inorganic particles like Al_2O_3, $BaTiO_3$, Li transition metal oxides, or Pt catalysts, including small amounts of organic additives such as dispersants and binders[1–8]. Dispersants play a role in uniformly dispersing the particles by covering ionic groups like carboxylic acids onto the particle surfaces, enhancing affinity to the solvent and electrostatic repulsion[3]. Conversely, binders act as cross-linking agents between individual particles, forming a network structure in the solvent (Fig. 1a)[3,5,6]. The interaction between particles and binders determines the structural stability of the network and is essential to impart the desirable formability in all liquid-phase processes such as tape-casting[2,7], inkjet printing[1,8], extrusion or filtration moulding[1,3,5], and binder jetting[1,3]. However, local disruptions and agglomerations in the network structure lead to non-uniform drying behaviour, resulting in defects including internal pores, deformations, and cracking[5,9]. Since these defects persist into subsequent processing steps of laminating, sintering, and so on, they become primary causes of performance degradation[1–3,8]. Consequently, slurry formulation has traditionally relied on years of intuition and experience to strict control. Nevertheless, the characteristics of slurry remain elusive, and even the assessment of its quality is not fully understood[1,4]. Therefore, quantitatively elucidating the particle–binder interactions in slurries is a key factor in optimizing the manufacturing process in diverse materials developments, including the electronics, environmental resources, and energy fields.

The characteristics of slurries are primarily interpreted from a rheological perspective[10–12]. Rheology comprehensively characterizes multiple aspects of slurries, including fluidity, viscoelasticity, structure stability, and stress relaxation[10–13]. Nevertheless, the obtained properties are a complex mixture of various factors such as dispersion

[1]Nano Carbon Device Research Center, National Institute of Advanced Industrial Science and Technology, Tsukuba 305-8565, Japan. [2]Health and Medical Research Institute, National Institute of Advanced Industrial Science and Technology, Tsukuba 305-8566, Japan. [3]Nanomaterials Research Institute, National Institute of Advanced Industrial Science and Technology, Ikeda 563-8577, Japan. [4]Multi-Material Research Institute, National Institute of Advanced Industrial Science and Technology, Nagoya 463-8560, Japan. [5]Research Institute for Sustainable Chemistry, National Institute of Advanced Industrial Science and Technology, Tsukuba 305-8565, Japan. ✉email: nakajima.h@aist.go.jp; toshi.okazaki@aist.go.jp

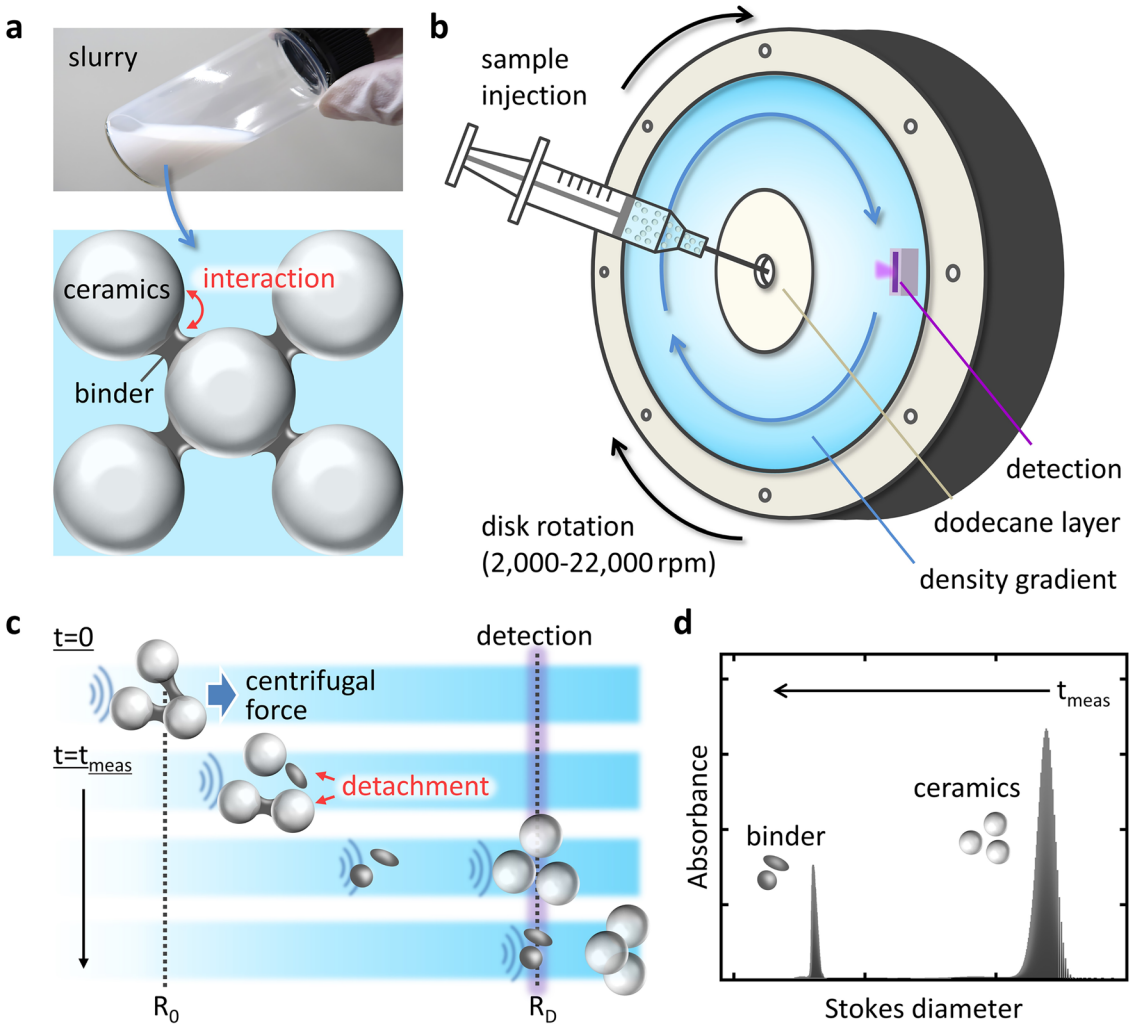

Figure 1. Conceptual diagram of this study. (**a**) Ideal network structure of particles and binders dispersed in a slurry. (**b-d**) Schematics of the DCS measurement. Arrival process of separated particles and binders to the detector (**c**) and the obtained spectrum (**d**).

state[11,12], interfacial tension[10,11], and interparticle attraction or friction[10,14,15], making the particle–binder interactions difficult to discern within this complexity. From another perspective, sedimentation tests[16,17] and solvent relaxation nuclear magnetic resonance (NMR)[18] are often employed. The former allows estimating the amount of binder adsorption to the particle surface by distinguishing between adsorbed and excess components in the slurry. The latter enables a qualitative examination of the adsorption characteristics of the binder to particles based on changes in the relaxation time of solvent protons. Recently, access to the interaction between Si particles and polyacrylic acid binders has been explored by using ultra-small-angle neutron scattering[19]. This method can estimate the length and shape of the polymer chains from the scattering spectrum, enabling the identification of binder aggregation near particles. However, these methods are based on a static approach and are limited in their ability to quantitatively evaluate the binding forces between particles and binders.

As a dynamic method for evaluating interactions between particles and binders, an atomic force microscopy (AFM)-based colloidal probe technique has been developed[20–25]. It involves attaching target particles (e.g., Al_2O_3) to the tip of a probe, and the interaction with the binder in the liquid medium can be directly measured from the force curves. Although numerous reports have demonstrated nano-Newton-order attractive adsorption interactions[20–25], these studies have limited microscopic verification focusing on individual particles. Consequently, there is still a lack of quantitative evaluation techniques to elucidate bulk interactions functioning across the entire slurry.

Differential centrifugal sedimentation (DCS)[26] is a measurement technique for evaluating particle size distribution based on the settling time of suspended particles (Fig. 1b). The technique combines centrifugal separation of particles with light scattering measurements at a specific detection position. Generally, the disk is filled with a sucrose solution capped with a dodecane layer, creating a density gradient through the rotation of the disk. Particles injected into the disk rotating at a constant angular velocity undergo centrifugal force (Supplementary Section 1). They are guided from the initial position R_0 to the detection position R_D and detected as light scattering

(Fig. 1c). The settling velocity depends on the size, density, and shape of the particles, and the equivalent sphere diameter (Stokes diameter) D_S is given by Eq. (1), according to Stokes' law.

$$D_s = \sqrt{\frac{18\eta \ln(R_D/R_0)}{(\rho - \rho_0)\omega^2 t_{meas}}} \quad (1)$$

where η is the viscosity of the fluid medium, ρ is the density of the particles, ρ_0 is the density of the fluid medium, ω is the angular velocity of the rotating disk, and t_{meas} is the time until reaching the detector. This method, based on centrifugal classification, has superior resolution over a wide range from a few μm to a few nm compared to other methods such as dynamic light scattering (DLS) and particle tracking analysis (PTA)[27]. Therefore, DCS has been applied for a variety of nanomaterials ranging from silica particles[28], metal nanoparticles[29], amyloid fibrils[30], carbon nanotubes[31–33], mineral dusts[34], and viruses[35]. In recent years, it has been found that the analysis allows for the extraction of various characteristics, such as settling coefficient[30], density[35], and porosity[32,33], based on Eq. (1).

Here, we provide a novel dynamic approach for evaluating adsorption interactions between particles and binders entangled in Al_2O_3 ceramic slurries by leveraging the measurement principle of DCS. In a centrifugal force field, inorganic particles and organic binders are separated from each other due to unbalanced size and density differences and are detected at separate arrival times (Fig. 1c,d). On the other hand, in a dispersed system where binders strongly adsorb to particles, the binders settle within the disk without separation. These dynamics enable quantitative analysis of the adsorption interactions on the order of nN. Based on the DCS results, we discuss the particle–binder interactions from multidimensional perspectives, including rheological properties and sheet formability.

Results

Fundamental properties of slurry

High-purity α-Al_2O_3 fine ceramic material with an average diameter of 3 μm was selected as the universally used sphere-like particles. The slurry was prepared using distilled water as a solvent (pH = 6), polycarboxylic acid as a dispersant, and an emulsion-type polymer binder composed of polymethylmethacrylate (PMMA) and polybutyl acrylate (PBA) (see "Methods" and Supplementary Section 2 in detail). By introducing a suitable amount of dispersant to the Al_2O_3 surface before the addition of binder, electrostatic repulsion among the particles is induced[36,37], ensuring a well-dispersed state with low viscosity[3,16] (Fig. 2a). Upon adding the binder to the dispersion, the acrylic emulsion induces wetting on the carboxylic acid surface layer, forming particle bridging through capillary forces[38,39]. The amount of binder absorbed on the Al_2O_3 surface is described by the Langmuir adsorption model related to the loading amount (Fig. 2b). The experimental results are adequately explained by the model, converging to a saturated adsorption amount (~ 4.5 wt%) in the high-concentration region. It suggests a uniform adsorption behaviour without precipitation or aggregation of active sites[40]. Furthermore, the saturated adsorption amount of ~ 4.5 wt% corresponds to ~ 80 mg/m^2 considering the specific surface area of Al_2O_3 particles (0.56 m^2/g). It is significantly higher than the one of a commonly used polyvinyl alcohol (PVA)-type binder on Al_2O_3 surface[16,41] (< 10 mg/m^2, Supplementary Fig. 9), indicating well-adsorptive properties of the binders. These details are described in Supplementary Section 2.5. It is noted that the surface potential (zeta potential) of Al_2O_3 particles before binder addition stabilizes at − 60 mV (Fig. S5), while the potential shifts to − 90 mV after binder addition (Fig. S12). It suggests that the adsorption of the binder on the Al_2O_3 surface is mainly due to electrostatic interactions.

Spectral characteristics of DCS measurements

Next, we examine the details of the spectral characteristics in the DCS measurements. Figure 3a presents DCS spectra from ceramics alone, binder alone, and a 10 wt% binder concentration slurry. The Stokes diameter corresponds to calculated values at the densities of Al_2O_3 (3.95 g/cm^3) and binder (1.10 g/cm^3). In ceramics alone, a single distribution with a peak at 3 μm is observed, which is in good agreement with the particle size in the scanning electron microscope (SEM) image (Supplementary Fig. 4). For the binder alone, a distribution with a Stokes diameter of ~ 300 nm is obtained. It suggests that DCS reflects the size of emulsion particles in the binder, as it aligns well with the particle size observed using SEM-based scanning electron-assisted dielectric microscope (inset in Fig. 3a).

Considering the above results, the DCS spectrum of the slurry shows that the peaks for ceramics and binder appear separately (bottom in Fig. 3a). To further investigate this behaviour, a sedimentation test was conducted (Fig. 3b). By diluting the slurry 10 times and allowing it to settle spontaneously, excess binder component (supernatant) and binder-adsorbed ceramic component (sediment) are separated (#1-#10 of bottom in Fig. 3b). Figure 3c illustrates the DCS spectra for each component. In the supernatants (#1 to #8), a peak corresponding to the binder is obtained. It is consistent with energy dispersive X-ray spectroscopy (EDS) analysis in SEM, where binder-derived carbon elements dominate (top in Fig. 3d). In the DCS spectrum of #9, although the binder peak is dominant, a small peak is observed in the few μm regions at 1.10 g/cm^3 equivalent. SEM–EDS analysis confirms the presence of a trace amount of Al_2O_3 particles in the excess binder (middle in Fig. 3d). Therefore, the detection of a small DCS peak suggests the existence of Al_2O_3 particles entrained in a large amount of binder. In contrast, the DCS spectrum of sediment #10 shows peaks for both ceramics and binder (bottom in Fig. 3c). SEM–EDS image reveals that the binder exists as an adsorbed component between Al_2O_3 particles (bottom of Fig. 3d). Additionally, the elemental composition analysis (Fig. 3e) shows a binder-derived carbon component of ~ 4 wt%, consistent with the binder adsorption analysis (Fig. 2b). However, in the DCS measurement, the binder and ceramics appear as separate peaks. It indicates that binder molecules adsorbed on the Al_2O_3 surface are detached by the centrifugal force field of DCS.

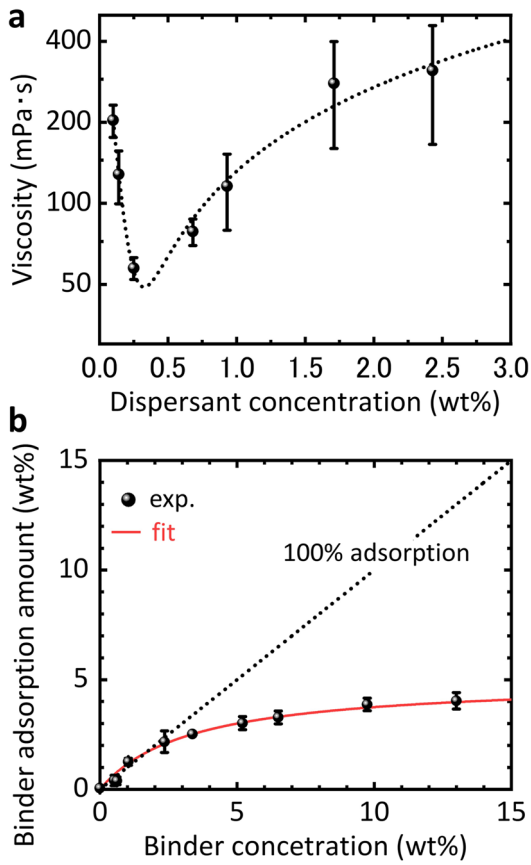

Figure 2. Fundamental properties of Al_2O_3 ceramic slurry. (**a**) Viscosity profile as a function of dispersant concentration. (**b**) Analysis of binder adsorption amount relative to preparation concentration.

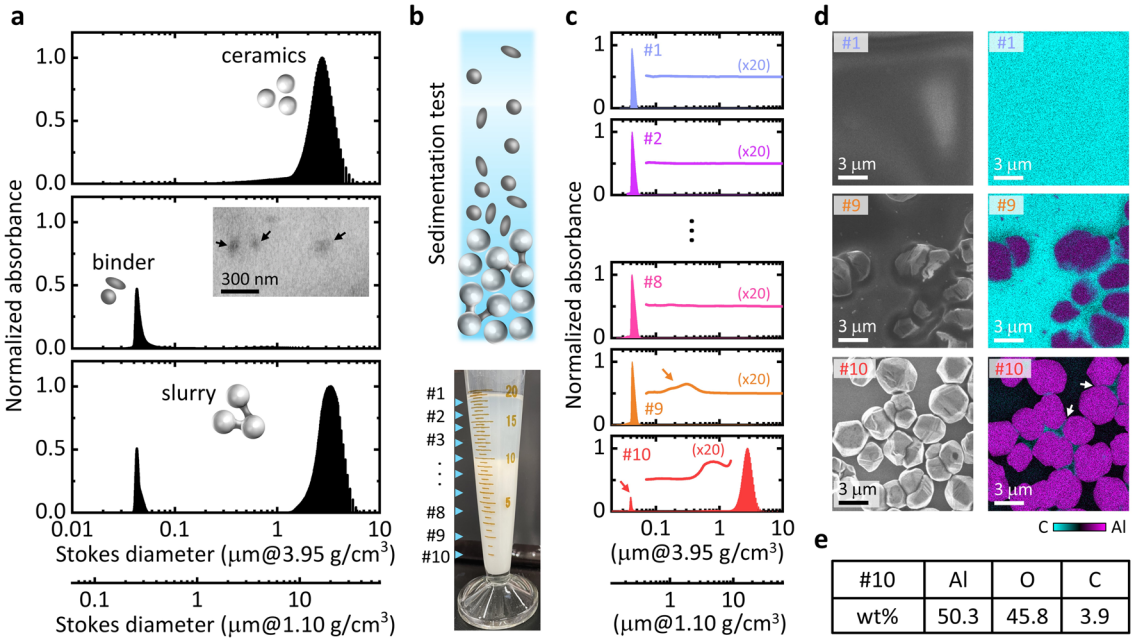

#10	Al	O	C
wt%	50.3	45.8	3.9

Figure 3. Detailed analysis of DCS spectra. (**a**) DCS spectra of Al_2O_3 particles, binder, and slurry, respectively. (**b**) Sedimentation test of slurry and (**c**) DCS profile obtained for each component #1-#10. (**d**) SEM–EDS images of #1, #9, and #10. (**e**) Weight concentration of Al, O, and C elements from SEM–EDS analysis of sediment (#10).

DCS profile reflecting particle–binder interactions

The interaction between particles and binders depends on various parameters such as the surface state of the particles and the type of polymers[5,11,16,17]. While the details of these effects will be discussed later, DCS measurements can identify changes in binder adsorption forces from detachment behaviour in a centrifugal force field. As a validation experiment, a slurry with a low concentration of binder of 0.8 wt%, where the excess binder component is sufficiently negligible (see Fig. 2b), was used. By varying the powder concentration, particle–binder interactions were controlled (Fig. 4a-c). The average particle distance $\overline{L^*}$ (normalized by particle size) and the number of contacts between particles $\overline{N}$ in spherical particles are simply described as $2/(3\phi)$ and 7ϕ, respectively, as a function of powder concentration ϕ (details in Supplementary Section 3.1)[42]. Figure 4a presents the calculated results for $\overline{L^*}$ and $\overline{N}$. At a powder concentration of 15 vol%, the particles are widely spaced ($\overline{L^*}$=4) and the number of contacts is limited ($\overline{N}$=1). In contrast, at 35 vol%, particles begin to contact with more than two other particles ($\overline{N}$=2.1). At concentrations exceeding 55 vol%, $\overline{N}$ values increase to 3.85 (55 vol%), 4.06 (58 vol%), and 4.34 (62 vol%), forming a robust network structure. Simultaneously, $\overline{L^*}$ decreases to 1.21 (55 vol%),

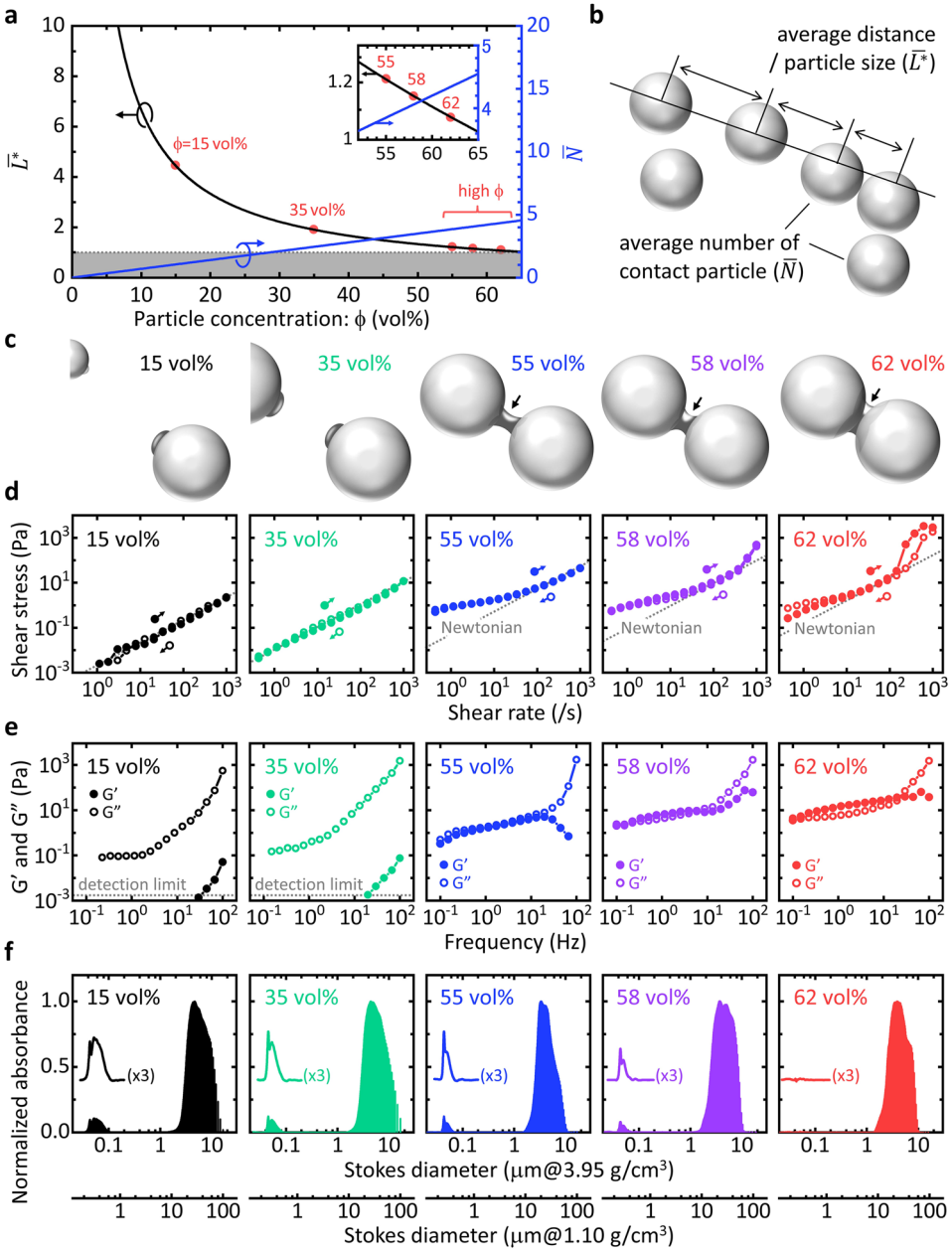

Figure 4. Experimental verification of particle–binder interactions. (**a**-**b**) $\overline{L^*}$ and $\overline{N}$ as a function of ϕ. (**c**) Variation of binder adsorption state with particle concentration. (**d**) Steady-state flow curves and **e** dynamic viscoelastic profiles for a series of slurries. (**f**) Change of DCS spectra depending on particle concentration.

1.15 (58 vol%), and 1.08 (62 vol%), indicating high filling. As the distance decreases, the binders bridging between the particles form thick necking structures (Fig. 4c). At this point, the binding force F between the particles and the binder is described by Eq.(2)[43].

$$F = \sigma_b \cdot A_0 \tag{2}$$

where σ_b is the strength of the binder and A_0 is the adsorption cross-sectional area between the particle and the binder. Consequently, the particle–binder interactions strengthen with increasing powder concentration. Utilizing this property, the binder detachment behaviour in DCS measurement is investigated. Note that for all slurries from 15 to 62 vol%, the binder adsorption amount on the Al_2O_3 surface is almost 100% (Supplementary Section 3.3).

First, based on the rheological behaviour of each slurry, the network structure of the particles is discussed. Figure 4d represents the steady-state flow curves. Slurries with powder concentrations of 15 and 35 vol% behave as Newtonian fluids (gray dotted line). On the other hand, those with concentrations above 55 vol% show pseudoplastic flow (shear thinning) at the low shear rate region (< 100/s), suggesting the formation of network structures[10–12]. Additionally, at 58 and 62 vol%, dilatancy (shear thickening) is observed at the high shear rate (> 200/s). This phenomenon arises from the strong resistance due to particle–particle friction in densely packed liquid under increasing shear rates, leading to a transition from shear thinning to shear thickening (jamming transition)[14,44]. The transition points correspond to 600/s and 150/s at 58 vol% and 62 vol%, respectively. This observation is a characteristic feature of highly concentrated slurries with narrow particle spacing. From these trends, it is evident that the rheology changes from liquid-like to solid-like as powder concentration increases. Moreover, for all powder concentrations, the slurries behave as Newtonian fluids under shear stress at ~ 100 Pa, corresponding to the stress at which the network structure cross-linked by binders is sufficiently disrupted.

More detailed structural information of a series of slurries is interpreted from dynamic viscoelasticity (Fig. 4e). G′ and G″ represent the storage and loss modulus, respectively. At 15 and 35 vol%, strong viscous profiles are exhibited regardless of frequency (G′ < G″). In contrast, at 55–62 vol%, elastic properties appear on the low frequencies (G′ ~ G″). As the frequency increases, viscous behaviours become dominant, and G″ tends to exceed G″ after 3, 8, and 30 Hz for 55, 58, and 62 vol%, respectively. These results indicate that the particle–binder interactions become stronger with increasing the powder concentration, forming a robust network structure. Like the steady-state flow curve (Fig. 4d), for all slurries, the network structure breaks down under shear stress of ~ 100 Pa, and the slurries behave as viscous fluids.

Changes in particle–binder interactions in these slurries are well characterized by DCS measurements (Fig. 4f). In slurries from 15 to 55 vol%, peaks derived from the binders are detected separately from the Al_2O_3 particles. In contrast, at 58 and 62 vol%, the peak intensity of the detected binder significantly decreases. Particularly at 62 vol%, the binder signal almost disappears. It suggests that the binder adsorption forces sufficiently resist the centrifugal force to allow the binder to settle with the Al_2O_3 particle in the rotating disk. Such dynamics are not observable with other particle sizing methods like DLS and are not discernible from surface charge measurements such as zeta potential (Supplementary Fig. 12). It represents unique insights afforded by the DCS method utilizing centrifugal force fields.

The detachment behaviour of binder particles due to centrifugal forces can assess the adsorption force of the binder on the Al_2O_3 surface because it varies with the rotation speed of the disk (i.e., centrifugal acceleration). Figure 5a illustrates the rotation speed dependence of the DCS spectra for each slurry from 15 to 62 vol%. For concentrations from 15 to 55 vol%, the intensities of the binder peak (integrated value) remain nearly constant regardless of the rotation speed (Fig. 5b). It suggests that the binders are almost detached from the Al_2O_3 particles even at low rotational speeds (2000 rpm). On the other hand, at 58 vol%, the intensity of the binder peak enlarges as the rotational speed is increased from 2000 to 4000 rpm. This trend is particularly pronounced at 62 vol%. The binder peaks, undetected at 2000 and 3000 rpm, gradually increase with higher rotation speeds from 4000 to 7000 rpm. It suggests that an increase in centrifugal acceleration leads to the detachment of adsorbed binders from the Al_2O_3 particles, which is good evidence of reflecting particle–binder interactions.

Influence of particle–binder interaction on sheet formability

Before the detailed analysis of DCS, the sheet formability of a series of slurries is discussed. Figure 6a illustrates the appearance of green sheets made from each slurry by the tape casting. At 15 and 35 vol%, the shape of sheets is not retained due to significant drying shrinkage. It is attributed to the rapid agglomeration of particles during drying caused by the high surface tension of water (~ 72 mN/m), which is commonly observed in weak network structures at low powder concentrations. In contrast, at 55 and 58 vol%, the robust network structure preserves particle alignment during drying, resulting in good sheet formability. Conversely, at 62 vol%, the coating property significantly degrades due to strong shear thickening (see Fig. 4d). Thus, the sheet formability of the slurry is closely associated with its rheological properties.

Particle–binder interactions strongly impact the microstructure and mechanical properties of the sheet. Figure 6b,c show the internal structures (cross-sectional SEM) and the results of nanoindentation measurements of each sheet, respectively. In the SEM images, it is evident that the binder connects among particles, forming a network structure (yellow arrows). These necking sites are formed with diameters ranging from 0.2 to 0.6 μm from 15 to 55 vol% (Supplementary Fig. 15). On the other hand, as the concentration increases to 58 and 62 vol%, the spaces between Al_2O_3 particles become narrower and the necking structures become thicker. These changes directly reflect the mechanical property of the sheet (Fig. 6c). Compared to the load–displacement curves at 15 to 55 vol% with a thin necking structure, there is a significant increase in hardness at 58 and 62 vol% with robust necking structures. At this point, the Young's modulus E of the sheet depends on the following parameters (details in Supplementary Section 3.4)[45].

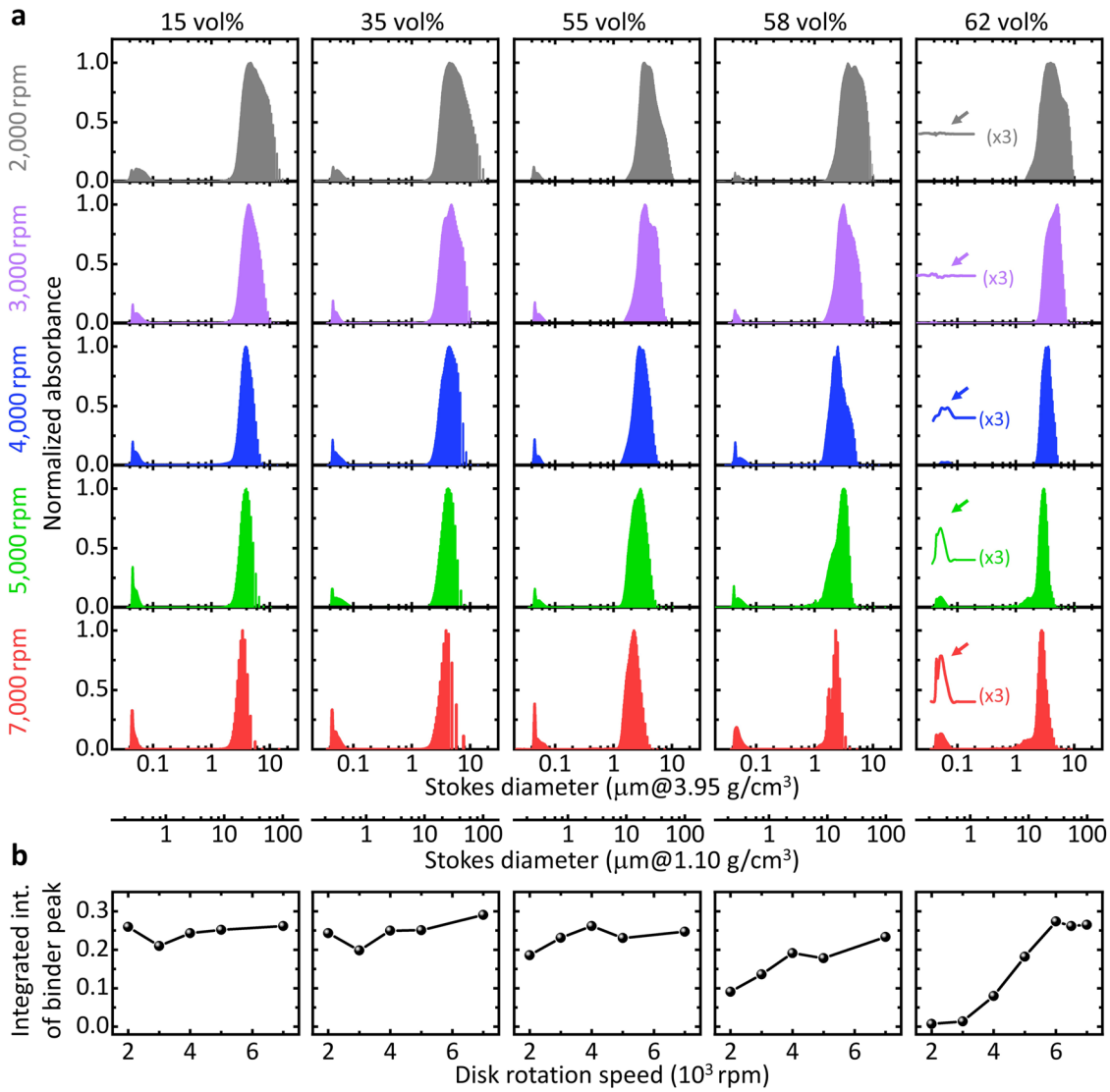

Figure 5. DCS profile dependence on disk ration speed. (**a**) DCS spectra of the 5 slurries at each disk rotation speed. (**b**) The change in integrated intensity of the binder peaks.

$$E \propto (1-\varepsilon)^3 \left(\frac{d_0}{D_c}\right)^2 \tag{3}$$

where ε is the porosity, d_0 is the diameter of the adsorption site between particles and binder, and D_c is the diameter of the ceramic particles. Equation 3 indicates that even in a system composed of particles with the same diameter, Young's modulus varies proportionally with the relative density $1-\varepsilon$ and the diameter of necking site d_0. The relative density of each sheet shows no significant differences among samples, being 60 ± 2% (15 vol%), 60 ± 2% (35 vol%), 61 ± 3% (55 vol%), 65 ± 2% (58 vol%), and 65 ± 4% (62 vol%) (Fig. 6d). In contrast, d_0 clearly changes with increasing powder concentration (Fig. 6e: details of the analysis in Supplementary Fig. 15). Moreover, this trend adequately explains the differences in Young's modulus of the sheets (Fig. 6f) from the relatively low values ~ 0.6 GPa at 15 to 55 vol% to the increased values of 1.3 and 2.9 GPa at 58 and 62 vol%, respectively. These results suggest that the particle–binders interaction directly influences the mechanical properties of green sheets.

Quantitative analysis of particle–binder interactions

Based on the experimental results obtained so far, the particle–binder interaction can be quantitatively assessed. Figure 7a shows a replot of the intensity change of the binder signal obtained from the disk rotation speed dependency (Fig. 5b) as a function of centrifugal acceleration $\omega^2 R$. Here, R is the rotation radius of the disk (details in Supplementary Section 3.5). Considering the relationship between the centrifugal force and the viscous resistance to Al_2O_3 particles and binders, the detachment behaviour of the binders can be appropriately

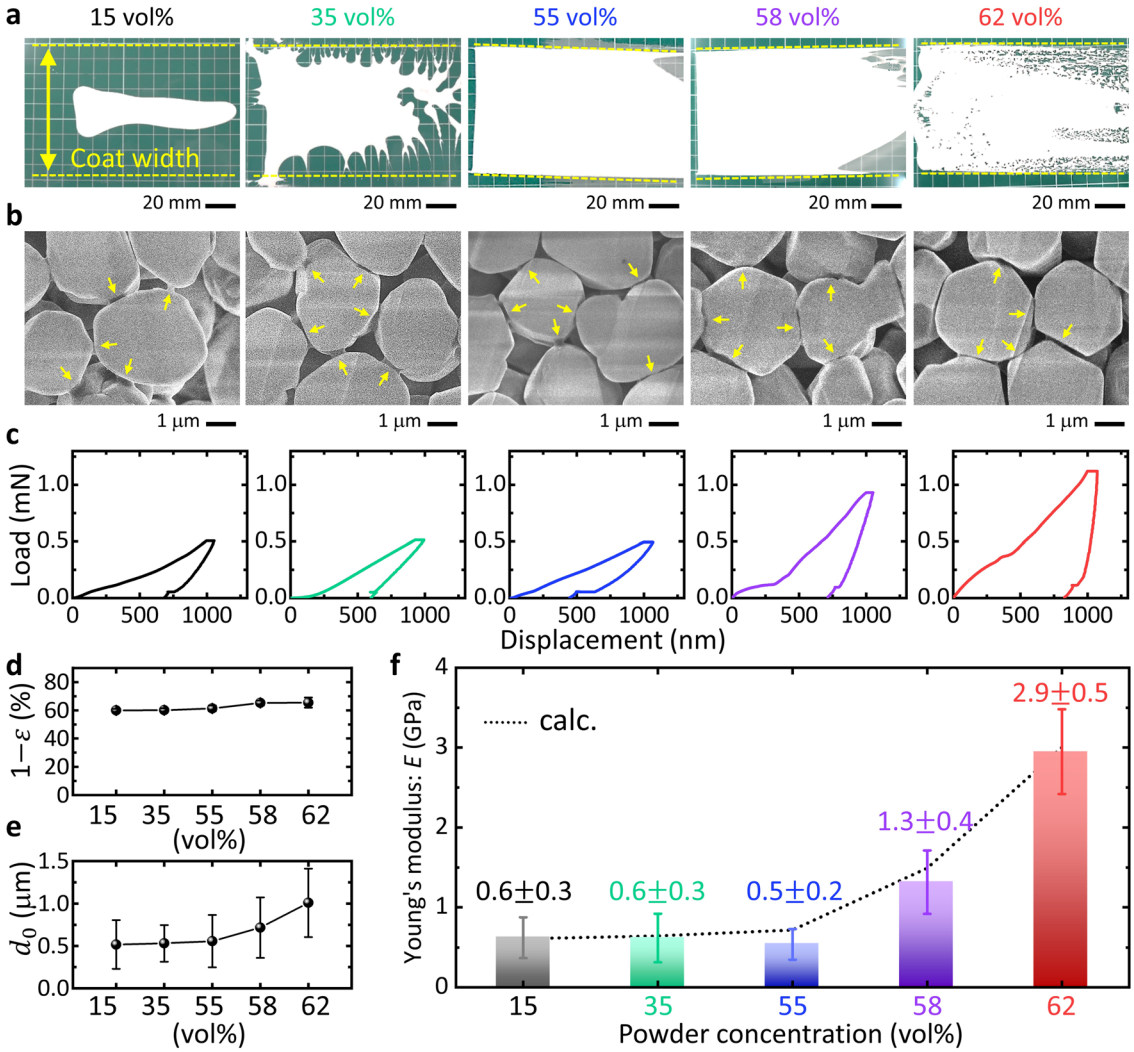

Figure 6. Changes in sheet formability of slurry. (**a**) Photographs of each green sheet. (**b**) Internal structures of the sheets (cross-sectional SEM). (**c**) Results of the nanoindentation test. (**d**) Relative density ($1-\varepsilon$). **e** Diameter distribution of the adsorption sites between particles and binder (d_0). (**f**) Change in Young's modulus.

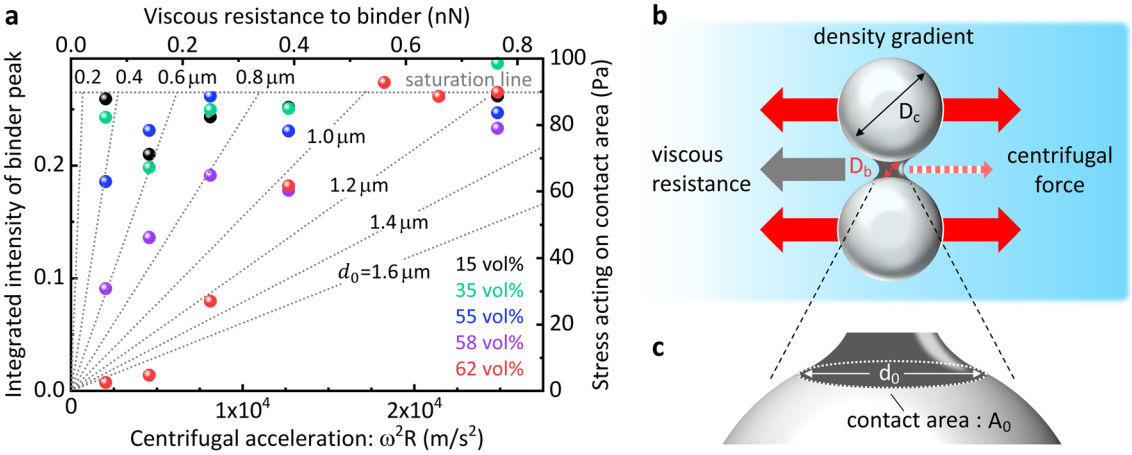

Figure 7. Quantitative analysis of particle–binder interactions. (**a**) Analysis results for the intensity change of binder peak obtained from the disk rotation speed dependence of DCS (Fig. 5b). (**b-c**) Analytical model. (**b**) Centrifugal force and viscous resistance acting on the particle and binder and (**c**) adsorption structure between the particle and binder.

interpreted (Fig. 7b). Ceramic particles injected into the rotating disk are subjected to a centrifugal force F_c proportional to the centrifugal acceleration described by Eq. (4).

$$F_c = \frac{\pi}{6} D_c^3 (\rho_c - \rho_0) \omega^2 R \tag{4}$$

where ρ_c is the density of ceramic particle (3.95 g/cm^3). In this experiment, the density difference between ceramics and the fluid medium ($\rho_c - \rho_0$) corresponds to 2.91 g/cm^3 and the diameter of ceramic particle D_c is 3 µm. On the other hand, when converting these parameters to binder molecules, the density difference with the fluid medium is 0.06 g/cm^3 and the diameter is 0.3 µm (Fig. 3a). It implies that the centrifugal force acting on the binder molecules is four orders of magnitude smaller than that on the ceramic particles. Therefore, the settling velocity of the binder-absorbed ceramic particles is determined by the centrifugal force of the ceramic particles themselves F_c. The terminal settling velocity v_c of ceramic particles is described by Eq. (5) according to Stokes' law.

$$v_c = \frac{D_c^2 (\rho_c - \rho_0) \omega^2 R}{18\eta} \tag{5}$$

Thus, the binder adsorbed on the ceramic particles settles within the disk while undergoing viscous resistance f_b proportional to v_c.

$$f_b = 3\pi D_b v_c \tag{6}$$

where D_b is the diameter of binder particles. The upper axis in Fig. 7a represents the viscous resistance f_b experienced by the binder, converted from the centrifugal acceleration $\omega^2 R$ (Supplementary Section 3.5). The binders start to detach from the Al_2O_3 surface due to the viscous resistance becoming greater than the binder's adhesion force (Eq. 2). For instance, in the case of the 62 vol% slurry, the binders are gradually detached as the viscous resistance increases from 0.2 to 0.4 nN. Upon reaching a viscous resistance of 0.6 nN, the detachment saturates. This value well aligns with a previous study that measured the interaction between the α-Al_2O_3 surface and methylcellulose binder using AFM (adhesion force ~ 0.5 nN)[21,22], suggesting a reliable analysis result.

The differences in binder detachment behaviour in slurries from 15 to 62 vol% can be understood by considering the necking structures of the binders (diameter d_0) (Fig. 7c). Since the adhesion force between particle–binder is described by the product of the binder's strength and the contact area (Eq. 2), it depends quadratically on d_0. Therefore, the durability against viscous resistance f_b varies with the square of d_0. The dotted line in Fig. 7a represents calibration curves using the estimated d_0 values from cross-sectional SEM observations of the sheets (Fig. 6e). Thin necking with d_0 of 0.4–0.6 µm was observed from 15 to 55 vol%, while thick necking with d_0 of ~ 0.8 µm and ~ 1 µm was observed at 58 and 62 vol%, respectively (Fig. 6b). These trends well correlate the results of DCS. From these calibration curves, the stress acting per unit area of the adhesion site $f_b/A_0 = f_b/\pi \left(\frac{d_0}{2}\right)^2$ can be determined (right axis in Fig. 7a). For instance, considering a viscous resistance of 0.2 nN to the thin necking site with d_0 of 0.4–0.6 µm, a strong stress > 100 Pa is applied to the contact area. Thus, adsorbed binders are easily detached (15 to 55 vol%). Conversely, assuming thick necking with d_0 of 0.8–1.0 µm, the stress drops < 50 Pa, allowing adsorbed binders to endure detachment sufficiently (58 and 62 vol%). From this perspective, the region of high centrifugal acceleration (> 20,000 m/s^2), where binder detachment occurs in all slurries, corresponds to an applied pressure of 80–100 Pa. It is in good agreement with the rheological properties, supporting that all slurries behave as Newtonian fluids under a shear stress of 100 Pa (Fig. 4d,e). Based on these consistencies, we can conclude that the analysis of binder detachment behaviour under the centrifugal force field of DCS allows for the quantitative evaluation of the particle–binder interactions in slurries.

Discussion

We have exemplified a dynamics method for assessing the interactions between particles and binders through the utilization of DCS. In water-based Al_2O_3 slurries where particle spacing was controlled by powder concentration, DCS yielded unique spectral changes directly reflecting the interactions within the slurry. Our results suggest that the binder's adsorption force, sensitive to the contact area between particles and binders, governs the overall interactions and rheological characteristics of the slurry. Furthermore, these interactions leave a history as the microstructure and mechanical properties of the green sheet. Although such insights have been semi-empirically inferred[1,9,46], experimental evidence is not yet abundant. For instance, attention has often been directed at the mechanical strength of green sheets, and variations in properties due to binder type or concentration have been reported[47,48]. Nevertheless, there is a still lack of methods to evaluate the interactions within slurries, making it challenging to comprehensively interpret the correlation from slurry to sheet.

DCS allows for the quantitative assessment of interactions that govern the overall properties of slurry from the detachment behaviour of binders. Thus, it provides robust support in understanding particle–binder interactions that vary with particle shape, size, and surface state. Additionally, DCS is adaptable not only to the emulsion-type binder, as used in this study, but also to various types of binders, such as PVA and polyvinyl butyral (PVB) (Supplementary Fig. 20). It leads to insights into the differences in dispersibility and sheet formability depending on binder types. Our results are expected to serve as a novel evaluation tool supporting the understanding and design of slurries, applicable to a wide range of material systems, including fine ceramics, lithium-ion batteries, and fuel cells.

Methods

Sample

Slurry fabrication

All materials used in this study were commercially available. The Al_2O_3 particles were high-purity α-crystalline powder (AA3, Sumitomo Chemical). The dispersant was a wetting agent consisting of a polycarboxylic acid copolymer (CA, Hichem). The solvent was distilled water, and the binder was an acrylic emulsion primarily composed of PMMA and PBA. The slurry was prepared by adding distilled water and dispersant to the Al_2O_3 powder, stirring in a ball mill for 1 h, and subsequently adding binder. Detailed information on each material, including composition ratios, is provided in Supplementary Section 2.

Sheet coating

The adjusted slurry was coated using an automatic film applicator (Allgood). A Si-free-type hydrophilic polyethylene terephthalate (PET) film (Unipeel, UNITIKA) was used as the substrate, and the slurry was coated at a gap of 0.5 mm, a width of 80 mm, and a feed rate of 10 cm/sec. The coated slurry was then dried for 24 h under atmospheric pressure and room temperature. The appearance of the resulting green sheet was photographed using a digital camera. Details in preparation and analysis are given in Supplementary Section 3.4.

Characterization

DCS

All DCS measurements in this study were conducted using a disk centrifuge (CPS 24,000 UHR, CPS Instruments). The disk was filled with a sucrose solution using a gradient generator (CPS Auto Gradient AG300, CPS Instruments) and capped with a dodecane layer to prevent evaporation (Fig. 1b). The mass concentration of sucrose ranged from 8 to 24%. The formation of a density gradient stabilizes the settling of particles, ensuring high resolution and accuracy[49]. Measurements were performed by injecting 0.05 mL of slurry without dilution into a disk rotating at a constant angular velocity. Polyvinyl chloride spherical standard particles (CPS Instruments) were used as calibration particles. The disk rotation speed was variable from 2000 to 22,000 rpm, and the disk temperature during measurements remained below 30 °C irrespective of the rotation speed. Detailed information about measurements and analysis is given in Supplementary Sections 1 and 4.

Analysis of binder adsorption amount

The measurements of binder adsorption (Fig. 2b) were performed using a commonly employed method[50]. The slurry was centrifugally separated at 3000 rpm (~ 2000 G) for 30 min using a tabletop centrifuge (H-36, KOKUSAN), extracting the sediment as the ceramic components adsorbed with the binder. Subsequently, the dried sediment was subjected to the weight change measurement from 100 to 550 °C using a thermogravimetric analyser (NEXTA STA200RV, Hitachi High-Tech). The resulting weight loss was analysed as the solid content of the binder and dispersant adsorbed on the Al_2O_3 surface. Details are described in Supplementary Section 2.5.

SEM-based scanning electron-assisted dielectric microscope

Observation of the emulsion particles of the binder (inset in Fig. 3a) was conducted using a scanning electron-assisted dielectric microscope[51,52] based on a field emission SEM (SU5000, Hitachi). A binder solution diluted with water was enclosed in a homemade liquid folder consisting of W-coated SiN film. The lower side of the liquid folder was equipped with a preamplifier, detecting the potential changes induced by the transmitted electron beams. These potential changes reflect local dielectric constant differences in the aqueous solution. Compared to water with a dielectric constant of ~ 80, organic material usually has a lower dielectric constant (e.g., PMMA is ~ 4.3) and shields the transmitted electron beam signals. Thus, emulsion particles suspended in an aqueous solution are observed as a dark contrast. The measurement was conducted at an acceleration voltage of 5 kV. Details are described in Supplementary Section 2.4.

SEM and EDS

SEM–EDS measurements (Fig. 3d) were performed using a field emission SEM (SU8220, Hitachi) equipped with an annular-type EDS detector (Quantax FlatQUAD, Brucker)[53]. Each component from the supernatant to the sediment (#1, #9, and #10) was dropped onto a conductive Si substrate and dried in air. The measurements were conducted at an acceleration voltage of 4 kV, and elemental composition analysis was carried out with ESPRIT analysis software. Cross-sectional SEM of the green sheet (Fig. 6b) was observed after processing with an ion milling device (IM4000, Hitachi High-Tech). In the processing, the sheet was sandwiched between two glass plates (both ends were fixed with resin to make a small gap between the sheet and the glass plates). After rough cross-sectional polishing using a manual polishing device (PLATO, TOP TECH), milling was performed under irradiation conditions with Ar ions at an acceleration voltage of 4 kV for 10 h. SEM observation was carried out at an acceleration voltage of 5 kV. Details are described in Supplementary Figs. 14 and 15.

Rheology

Rheological properties of a series of slurries were analysed at room temperature and atmospheric pressure using a modular compact rheometer (MCR 102, Anton Paar) equipped with a cone plate (diameter of 25 mm and gap of 250 μm). Viscosity changes as a function of dispersant concentration (Fig. 2a) were measured at a shear rate of 500/s. In the steady-state flow curve (Fig. 4d), shear rates from 0.5 to 10^3/s were set with a logarithmic slope for integration times of 10 s (0.5/s) to 1.5 s (10^3/s). Dynamic viscoelasticity (Fig. 4e) was measured at a fixed strain of 1%, integrating profiles from 0.1 to 100 Hz with an integration time of 1 s. It is noted that for all

slurries with powder concentrations ranging from 15 to 62 vol%, the condition of a 1% strain showed sufficiently linear trends for both G′ and G″, indicating measurements in a flow region without structural breakdown (Supplementary Fig. 11).

Nanoindentation
The mechanical strength of the green sheets (Fig. 6c) was evaluated using a nanoindenter (iNano, KLA). The sheet was fixed to an Al substrate at four edges with acrylate adhesive, and measurements were performed using a Berkovich-type diamond indenter (typically $n > 30$). Load–displacement curves were measured at a set depth of 1 μm, and Young's modulus was calculated from the unloading profiles. The 1 μm indentation depth is sufficiently small than the thickness of the sheet (> 0.2 mm), and the influence of the substrate during measurements can be negligible (Supplementary Fig. 16). The conversion of Young's modulus from the load–displacement curve was performed using InView analysis software.

Relative density of sheets
The relative density of the green sheets (Fig. 6d) was evaluated using a precision electric balance (XPR225DRV, Mettler Toledo) and a laser microscope (SFT-4500, Shimadzu). The bulk density was calculated from weight and volume measurements using sheet fragments of ~ 0.5 mm square size, and the relative density was determined by dividing it by the ideal density.

Data availability
All data necessary to lead the conclusions of current study are available from corresponding authors upon request.

Received: 7 May 2024; Accepted: 23 July 2024
Published online: 09 August 2024

References
1. Chen, C. *et al.* Additive manufacturing of piezoelectric materials. *Adv. Funct. Mater.* **30**, 2005141 (2020).
2. Wang, G. *et al.* Electroceramics for high-energy density capacitors: current status and future perspectives. *Chem. Rev.* **121**, 6124–6172 (2021).
3. Chen, Y. *et al.* Porous ceramics: light in weight but heavy in energy and environment technologies. *Mat. Sci. Eng. R* **143**, 100589 (2021).
4. Duffner, F. *et al.* Post-lithium-ion battery cell production and its compatibility with lithium-ion cell production infrastructure. *Nat. Energy* **6**, 123–134 (2021).
5. Zhang, L. *et al.* Exploring more functions in binders for lithium batteries. *Electrochem. Energy Rev.* **6**, 36 (2023).
6. Dou, W. *et al.* Review on the binders for sustainable high-energy-density lithium ion batteries: status, solutions, and prospects. *Adv. Funct. Mater.* **33**, 2305161 (2023).
7. Mahmud, L. S., Muchtar, A. & Somalu, M. R. Challenges in fabricating planar solid oxide fuel cells: a review. *Renew. Sustain. Energy Rev.* **72**, 105–116 (2017).
8. Ahn, C.-Y. *et al.* Differences in the electrochemical performance of Pt-based catalysts used for polymer electrolyte membrane fuel cells in liquid half- and full-cells. *Chem. Rev.* **121**, 15075–15140 (2021).
9. Zhang, Y. S. *et al.* A review of lithium-ion battery electrode drying: mechanisms and metrology. *Adv. Energy Mater.* **12**, 2102233 (2022).
10. del Mazo-Barbara, L. & Ginebra, M.-P. Rheological characterisation of ceramic inks for 3D direct ink writing: a review. *J. Eur. Ceram. Soc.* **41**, 18–33 (2021).
11. He, Y. *et al.* Revisiting the electrode manufacturing: a look into electrode rheology and active material microenvironment. *J. Energy Chem.* **72**, 41–55 (2022).
12. Khandavalli, S. *et al.* Rheological investigation on the microstructure of fuel cell catalyst inks. *ACS Appl. Mater. Interfaces* **10**, 43610–43622 (2018).
13. Wang, Y. & Ewoldt, R. H. Thixotropy, antithixotropy, and viscoelasticity in hysteresis. *J. Rheol.* **67**, 1199–1219 (2023).
14. Conley, G. M. *et al.* Relationship between rheology and structure of interpenetrating, deforming and compressing microgels. *Nat. Commun.* **10**, 2436 (2019).
15. Nabizadeh, M. & Jamali, S. Life and death of colloidal bonds control the rate-dependent rheology of gels. *Nat. Commun.* **12**, 4274 (2021).
16. Romdhane, M. R. B. *et al.* Dispersion of Al_2O_3 concentrated suspensions with new molecules able to act as binder. *J. Eur. Ceram. Soc.* **24**, 2723–2731 (2004).
17. Kitamura, K., Tanaka, M. & Mori, T. Effects of the mixing sequence on the graphite dispersion and resistance of lithium-ion battery anodes. *J. Colloid Interface Sci.* **625**, 136–144 (2022).
18. Cooper, C. L. *et al.* The use of solvent relaxation NMR to study colloidal suspensions. *Soft Matter* **9**, 7211–7228 (2013).
19. Burdette-Trofimov, M. K. *et al.* Understanding binder-silicon interactions during slurry processing. *J. Phys. Chem. C* **124**, 13479–13494 (2020).
20. Khan, A. U. *et al.* The strength of colloidal interactions in the presence of ceramic dispersants and binders. *J. Mater. Chem.* **12**, 17430–21747 (2002).
21. Yilmaz, H. *et al.* Methyl cellulose bridging between alumina surfaces. *J. Ceram. Soc. Jpn.* **118**, 314–317 (2010).
22. Yilmaz, H. *et al.* Lateral and normal forces in polymer-mediated interaction of alumina surfaces. *J. Am. Ceram. Soc.* **94**, 3761–3767 (2011).
23. Isobe, T. *et al.* Adsorption and adhesion of poly(vinyl alcohol) and poly(ammonium acrylate) as organic additives for wet mold processing of Al_2O_3. *Ceram. Int.* **39**, 3857–3864 (2013).
24. Nguyen, Q. D., Oh, E.-S. & Chung, K.-H. Nanomechanical properties of polymer binders for Li-ion batteries probed with colloidal probe atomic force microscopy. *Polym. Test.* **76**, 245–253 (2019).
25. Lee, M. *et al.* In-operando AFM characterization of mechanical property evolution of Si anode binders in liquid electrolyte. *ACS Appl. Energy Mater.* **3**, 1899–1907 (2020).
26. Scott, D. J., Harding, S. E. & Rowe, A. J. *Analytical Ultracentrifugation: Techniques and Methods Ch.14* (Royal Society of Chemistry, Cambridge, 2005).
27. Anderson, W. *et al.* A comparative study of submicron particle sizing platforms: Accuracy, precision and resolution analysis of polydisperse particle size distributions. *J. Colloid Interface Sci.* **405**, 322–330 (2013).

28. Kamiti, M. *et al.* Simultaneous absolute determination of particle size and effective density of submicron colloids by disc centrifuge photosedimentometry. *Anal. Chem.* **84**, 10526–10530 (2012).
29. Knauera, A. *et al.* Au/Ag/Au double shell nanoparticles with narrow size distribution obtained by continuous micro segmented flow synthesis. *Chem. Eng. J.* **166**, 1164–1169 (2011).
30. Arosio, P. *et al.* Analysis of the length distribution of amyloid fibrils by centrifugal sedimentation. *Anal. Biochem.* **504**, 7–13 (2016).
31. Nadler, M. *et al.* Preparation of colloidal carbon nanotube dispersions and their characterisation using a disc centrifuge. *Carbon* **46**, 1384–1392 (2008).
32. Kato, Y. *et al.* Quantitative method for analyzing dendritic carbon nanotube agglomerates in dispersions using differential centrifugal sedimentation. *J. Phys. Chem. C* **123**, 21252–21256 (2019).
33. Kato, Y. *et al.* Porosity and size analysis of porous microparticles by centrifugal sedimentation with and without density gradient. *Powder Technol.* **407**, 117663 (2022).
34. McCutcheon, J. *et al.* Mineral phosphorus drives glacier algal blooms on the Greenland ice sheet. *Nat. Commun.* **12**, 570 (2021).
35. Neumann, A. *et al.* New method for density determination of nanoparticles using a CPS disc centrifuge. *Colloids Surf. B Biointerfaces* **104**, 27–31 (2013).
36. Megias-Alguacil, D. *et al.* Contact angle and adsorption behavior of carboxylic acids on α-Al_2O_3 surfaces. *J. Colloid Interface Sci.* **353**, 512–518 (2011).
37. Studart, A. R. *et al.* Unifying model for the electrokinetic and phase behavior of aqueous suspensions containing short and long amphiphiles. *Langmuir* **27**, 11835–11844 (2011).
38. Koos, E. Capillary suspensions: Particle networks formed through the capillary force. *Curr. Opin. Colloid Interface Sci.* **19**, 575–584 (2014).
39. Danov, K. D. *et al.* Hardening of particle/oil/water suspensions due to capillary bridges: experimental yield stress and theoretical interpretation. *Adv. Colloid Interface Sci.* **251**, 80–96 (2018).
40. Nakamura, K., Iwata, N. & Mori, T. Effects of eluted metal ions on the properties of ceramic slurry and slip-casted green bodies. *J. Asian Ceram. Soc.* **8**, 528–536 (2020).
41. Wiśniewska, M. *et al.* Investigation of the alumina properties with adsorbed polyvinyl alcohol. *J. Therm. Anal. Calorim.* **103**, 329–337 (2011).
42. Tsubaki, J. Geometrical analysis of particle system dispersed in liquid. *J. Chin. Inst. Chem. Eng.* **35**, 47–54 (2004).
43. Uhland, S. A. *et al.* Strength of green ceramics with low binder content. *J. Am. Ceram. Soc.* **84**, 2809–2818 (2001).
44. Hsu, C.-P. *et al.* Exploring the roles of roughness, friction and adhesion in discontinuous shear thickening by means of thermoresponsive particles. *Nat. Commun.* **12**, 1477 (2021).
45. Arató, P. *et al.* Mechanical properties in the initial stage of sintering. *J. Mater. Sci.* **30**, 1863–1871 (1995).
46. Nakajima, H. *et al.* Hidden correlation between rheological dynamics and crack formation in water-based slurry. *J. Eur. Ceram. Soc.* **44**, 4141–4149 (2024).
47. Gilmer, D. *et al.* An in-situ crosslinking binder for binder jet additive manufacturing. *Addit. Manuf.* **35**, 101341 (2020).
48. Yanez-Sanchez, S. I. *et al.* Model approach for binder selection in binder jetting. *Ind. Eng. Chem. Res.* **60**, 15162–15173 (2021).
49. Brakke, M. K. Zonal separations by density-gradient centrifugation. *Arch. Biochem. Biophys.* **45**, 275–290 (1953).
50. Iwata, N. & Mori, T. Effect of binder addition on optimum additive amount of dispersant for aqueous $BaTiO_3$ slurry. *Ceram. Int.* **45**, 19644–19649 (2019).
51. Ogura, T. Direct observation of unstained biological specimens in water by the frequency transmission electric-field method using SEM. *Plos One* **9**, e92780 (2014).
52. Okada, T. & Ogura, T. Nanoscale imaging of untreated mammalian cells in a medium with low radiation damage using scanning electron-assisted dielectric microscopy. *Sci. Rep.* **6**, 29169 (2016).
53. Nakajima, H. *et al.* Nonuniform functional group distribution of carbon nanotubes studied by energy dispersive X-ray spectrometry imaging in SEM. *Nanoscale* **11**, 21487–21492 (2019).

Acknowledgements

This work was based on results obtained from a project, JPNP22005, commissioned by the New Energy and Industrial Technology Development Organization (NEDO). We also thank Yumi Masuda for her technical support.

Author contributions

H.N. and T.O. conceived the research and designed the experiments. N.K. and R.U. prepared the slurry samples. H. N. performed the experiments and data analysis and wrote the manuscript. T.O. performed SE-ADM, and R.W. performed pyrolysis-GC/MS. Y.K. contributed to the theoretical analysis of the DCS measurements, and K.K. contributed to the methodology for rheological characterization. All authors discussed the results and commented on the manuscript.

Competing interests

The authors declare no competing interests.

Additional information

Supplementary Information The online version contains supplementary material available at https://doi.org/10.1038/s41598-024-68420-9.

Correspondence and requests for materials should be addressed to H.N. or T.O.